A Stiffness Controllable Multimodal Whisker Sensor Follicle for Texture Comparison

Hasitha Wegiriya[1], Nicolas Herzig[2], Sara-Adela Abad[3], S.M.Hadi Sadati[4], and Thrishantha Nanayakkara[5]

Abstract—Mammals like rats, who live in dark burrows, heavily depend on tactile perception obtained through the vibrissal system to move through gaps and to discriminate textures. The organization of a mammalian whisker follicle contains multiple sensory receptors and glands strategically organized to capture tactile sensory stimuli of different frequencies. In this paper, we used a controllable stiffness soft robotic follicle to test the hypothesis that the multimodal sensory receptors together with the controllable stiffness tissues in the whisker follicle form a physical structure to maximize tactile information. In our design, the ring sinus and ringwulst of a biological follicle are represented by a linear actuator connected to a stiffness controllable mechanism in-between two different frequency-dependent data capturing modules. In this paper, we show for the first time the effect of the interplay between the stiffness and the speed of whisking on maximizing a difference metric for texture classification.

Index Terms—Whisker sensors, Tactile sensors, Soft robotic sensor, Bio-inspired sensors, Stiffness controllable sensors, Multimodal sensors.

I. INTRODUCTION

TACTILE sensing hair or vibrissae (whisker) provides a rich sense of touch for several mammals. These mammals commonly use whiskers to determine texture, compliance, orientation, shape, size, and location of objects [1]. In several behaviors, whiskers differ from the regular pelage hair as detailed by A.S Ahl [2]. Furthermore, these whiskers are innervated by multiple mechanoreceptors [3] [4]. The follicle sinus complex (FSC) amplifies the vibrations of the whisker allowing the mechanoreceptors at the base to capture extremely small stimuli [5] [6]. Authors of [7] used psychophysical methods to investigate, how fixed head mice can localize an object along the axis of a single whisker and the stresses at the follicle relative to the stiffness of the whisker shaft.

All transduction occurs at the mechanoreceptors in the follicle. Each follicle comprises one whisker, deep vibrissal and superficial vibrissal nerves, ring sinus, Ringwulst and an outer collagenous capsule with arrector pili (involuntary muscles) [2] [6].

Hence, whiskers have gained the attention of several works about artificial tactile sensors. Most of the early designs of artificial whiskers use simple methods to examine an array organization and mechanical properties of the whisker. Therefore, whisker sensor designs used rigid whiskers with a means of calculating the change of angle with a potentiometer and a resistive transducer [8][9].

An over-complicated design with extra circuitry and wiring is not always essential when a similar outcome can be achieved using a series of simple devices [9]. As an example, capacitor microphones attached to a simple whisker sensor have been able to categorize between four different textures [10] with 70% success rate with a single sweep. Authors of [11] used simple designs including piezoresistive strain gauges to measure the two-dimensional deviation of four steel whiskers. They implemented a novel method in order to determine the contact point along its length by measuring the bending moment at the base of a whisker. Moreover, they were capable of getting an accurate map of the object in three-dimensions by circling the array around the object [11][12][13]. Authors of [14] replaced strain gauges with Hall effect sensors for the same technique and authors of [15] developed miniaturized piezoelectric MEMS flow whiskers sensors .

Authors of [12] developed a whisking pattern by having the least force impact as possible versus repeated contact. Although these works explain that a simple sensor setup can obtain good results, further work is needed to explore the potential of the whisker follicle dynamics to improve information [16]. The 'Biotact' sensor for classifying the surface textures is a recent advancement in this direction [17]. This bio-inspired sensor has the ability of actuation and control of the whisker, and the sensory part contains a small permanent magnet and Hall Effect device [17]. Additionally, [18] shows that robotic whiskers could be used for high fidelity tactile exploration for distinguishing object shapes and contours.

These examples focus on sensing modalities in order to capture sensory information and not on the design of the whisker follicle itself. Therefore, there is scope to investigate features such as an effect of stiffness control at the follicle level, the optimal range of stiffness and speed of whisking to capture more information.

[1] H. Wegiriya is with the Faculty of Natural and Mathematical Sciences, King's College London, London, WC2R 2LS, UK (e-mail: hasitha.wegiriya@kcl.ac.uk).
[2] N. Herzig is with the Automatic, Control and Systems Engineering Department, University of Sheffield, Amy Johnson Building, Portobello Lane, Sheffield, S1 3JD, United Kingdom, UK.
[3] S.A. Abad is with the Mechanical Engineering Department, University College London, Torrington Place, London, WC1E 7JE, UK. S.A. Abad is also with the Institute for Applied Sustainability Research, Av. Granados E13-55 e Isla Marchena, No.44, Quito, 170503, Ecuador.
[4] S.M.H. Sadati is with the Department of Surgical and Interventional Engineering, King's College London, UK.
[5] T. Nanayakkara is with Dyson School of Design Engineering, Imperial College London, Dyson Building, 25 Exhibition Road, London, SW7 2DB, UK.

Our previous work [19] introduced the role of the whisker indentation and the whisking speed for a bi-modal sensing whisker follicle in the task of distinguishing textures. The following paper aim is to show that variations of stiffness at the ring sinus level help to distinguish two lookalike textures. Furthermore, this paper demonstrates that variable stiffness and whisking speeds of a multimodal whisker follicle comprised of piezoelectric and Hall effect sensors have a major interaction effect to distinguish similar types of textures.

The structure of the rest of the paper follows: Section II-A presents the new design of the whisker with a controllable stiffness mechanism. In II-B and II-C the behavior of the sensors and the dynamic whisker model are described, respectively. Then, the experimental setup is presented in section II-D, before the presentation of the texture classification process in II-E. The results showing that this whisker follicle can be controlled in stiffness to sharpen the probability distribution of a difference metric are presented in III. This metric based on co-variation of the two kinds of sensory modality (Hall effect sensor and piezoelectric) seems suitable to distinguish two lookalike textures. A change in probability distributions helps to distinguish two similar textures such as two sandpapers with different grit level. The final section IV gives a discussion and concluding remarks of our findings.

II. DESIGN METHODS AND SENSOR STRUCTURE

In this paper, we test the hypothesis that stiffness control in a multimodal robotic whisker follicle can capture more information in different regions of the frequency spectrum of whisker vibrations.

A. Stiffness Controllable Whisker Sensor

The variable stiffness multimodal whisker follicle (VS-MWF) with two sensor modalities shown in Fig. 1 is an advancement from the constant stiffness multimodal whisker follicle (CS-MWF) reported in [19]. The VS-MWF is comprised of a 3D printed cylindrical body (CB), a soft silicone rubber (Ecoflex 00-10) joint (SJ), a rigid 3D printed whisker shaft base (WSB). This WSB contains a 2 mm diameter permanent magnet (PM), a 0.5mm diameter 200mm long carbon fiber shaft (CFWS), a Hall effect Sensor (HS), and a piezoelectric sensor (PS). The piezoelectric sensor is attached to the WSB while the carbon fiber shaft passes through the center of the piezoelectric sensor. The tip of the carbon fiber is attached to the permanent magnet. The latter is free to move in the WSB cavity since a 4 mm gap of between the cylindrical body and the piezoelectric sensor holder allows the WSB to oscillate when the whisker vibrates.

The stiffness controllable mechanism is comprised of four carbon fiber shafts (0.5 mm diameter and 17 mm length). These shafts slide into four equally spaced silicone tubes (1 mm internal diameter, 2 mm outer diameter) that are attached to the top of the WSB. A steering ring mechanism was designed to control the carbon fiber shafts so that all four carbon fiber shafts move into the silicone tubes when the ring rotates clockwise concentric to the WSB.
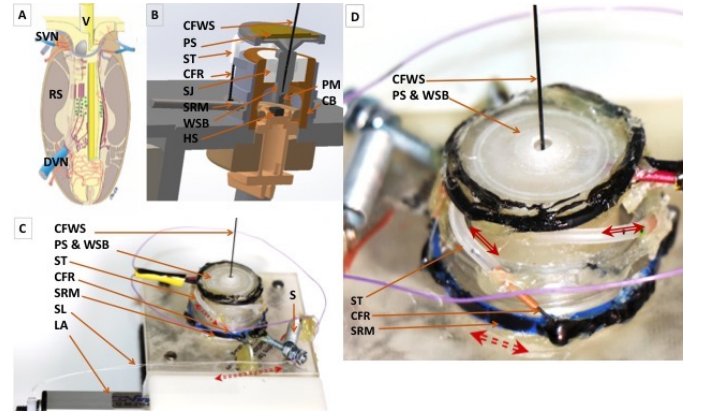

Fig. 1: Whisker follicle. (A) Schematic illustration of the structure innervation of a rat whisker follicle [20]; V, vibrissal shaft; RS, ring sinus and ringwulst; SVN, superficial vibrissal nerve; DVN, deep vibrissal nerve. (B) Cross section of the variable stiffness multimodal whisker follicle (VS-MWF); CFWS, carbon fiber whisker shaft; PS, piezoelectric sensor; ST, silicone tube; CFR, carbon fiber rod; SJ, silicone joint; SRM, steering ring mechanism; WSB, whisker shaft base; HS, Hall effect Sensor; PM, permanent magnate; CB, 3D printed Cylindrical body. (C) Complete VS-MWF; S, spring, SL, string link; LA, linear actuator. The spring is used to relocate the SRM when the LA is decreasing the actuated length. (D) Enlarged VS-MWF to demonstrate the stiffness controllable system.

The range of displacement of the carbon fiber shaft is from 0 to 3.2 mm in steps of 0.4 mm. In the rest of the paper, each step denotes a linear actuator pulling level where each of these levels comprises a WSB joint stiffness variation. Since the stiffness of the WSB joint increases when the carbon fiber shafts are moved into the silicone rubber tubes, the stiffness increases from 0.297 to 0.9738 N/mm. The steering ring is controlled by a Linear actuator Actuonix L12-50-210-6-l. The signals of both sensors and the position of the linear actuator are acquired and controlled through a National Instrument acquisition card (NI DAQ USB 6341).

In order to find the actual follicle stiffness at each step of pulling level, the ATI Nano17 force sensor and the Aerotech high precision linear stage (nanometer accuracy and repeatability) used to capture high accuracy force and movement data. Then the multiple readings of force data have taken for 2mm displacement of the follicle joint for each stiffness configuration. The stiffness of the follicle has computed by regressing force data and displacement data of the follicle.

B. Whisker Sensor Characterization

The sensitivity of the sensors depends on the vibration of the whisker shaft and the stiffness of the silicone joint. When the whisker shaft vibrates, the shaft and silicone joint deform. These deformations generate vibrations on the Piezoelectric Sensor (PS) and the Permanent Magnet (PM) inside the WBS. The piezoelectric sensor stress can be expressed by

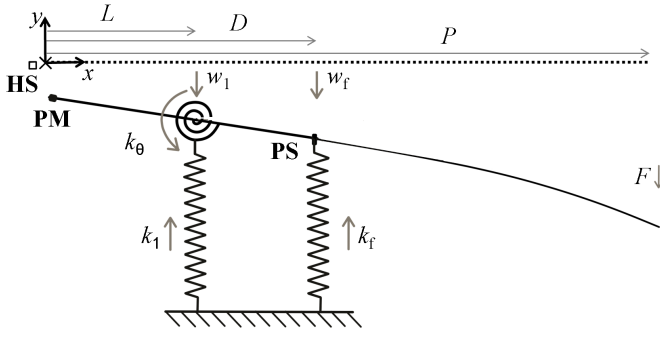$$\sigma_{\text{PS}} = F_{\text{PS}}/a_{\text{PS}}, \tag{1}$$

Fig. 2: Schematic diagram of the whisker follicle with a Hall effect sensor (HS), a Permanent magnet (PM), and a piezoelectric sensor (PS). The soft joint is represented by a torsion ($k_\theta = 200$N/rad) spring, a linear ($k_1 = 0.2$N/mm) spring at $x = L = 8$mm and a controllable stiffness spring (k_f) at $x = D = 13$mm. The applied force at the tip of the whisker is F. (x_0, y_0) is the model reference frame origin (shown with ($\times$) in the figure)
, the whisker overall length is $P = 213$mm. w_1 and w_f denote the beam lateral displacement at the silicone joint and the piezoelectric sensor respectively.

where $F_{\text{PS}} = k_f w_f$ is the lateral (shear) force exerting by the follicle on the piezoelectric disk, k_f is the variable stiffness of a spring in our simple model that simulates the disk lateral stiffness, w_f is this spring lateral deflection, and $a_{\text{PS}} = 0.5[\text{mm}^2]$ is the whisker-PS contacting area.

A cylindrical magnet is attached to the end bottom of the WSB. The magnet displacement generates a fluctuation in magnetic flux (B_{H}) around the Hall effect sensor. To calculate B_{H}, We assume that the magnet and follicle axes are aligned, and the hall sensor is placed and (considering the small deformation of the beam) remains along the magnet axis despite the magnet displacement. Then from the formula for the magnetic flux on the the symmetry axis of an axially magnetized cylinder magnet [21] we have,

$$B_{\text{H}} = \frac{B_{\text{r}}}{2}\left(\frac{l_{\text{PM}} + l_{\text{MH}}}{\sqrt{r_{\text{PM}}^2 + (l_{\text{PM}} + l_{\text{MH}})^2}} - \frac{l_{\text{MH}}}{\sqrt{r_{\text{PM}}^2 + l_{\text{MH}}^2}}\right), \tag{2}$$

where $B_{\text{r}} = 1.1$T is the residual magnetism of the cylindrical permanent magnet, $l_{\text{PM}} = 2$mm and $r_{\text{PM}} = 1$mm are the length and radius of the permanent magnet, respectively. l_{MH} is the PM-HS distance (see Fig. 2).

The variation of the electrical signals in PS and HS (Hall effect Sensor) can be related to the function of the superficial vibrissal nerve and the deep vibrissal nerve, respectively. The stiffness controllable silicone joint (k_f) mimics the ring sinus muscles in a biological whisker follicle. This controllable stiffness, as shown in section III, influence the sensor signals by changing the follicle vibration dynamics.

C. Whisker Modal Analysis

The whisker setup vibration dynamics is modeled as undamped modal analysis of a simple Euler-Bernoulli beam, with uniform cross-section and negligible axial strain and cross-section rotation compared to the beam shear strain. The relation between the external load and the whisker displacement and deformation can be expressed as follows [22]:

$$EI\partial^4 w/\partial x^4 + \rho a \partial^2 w/\partial t^2 = F(x,t), \tag{3}$$

where w is the beam lateral displacement, x is beam axial location, t is time, and $F(x,t)$ is the external load. $E = 228$GPa and $\rho = 1880$Kg/m^3 are the beam Elasticity modulus and density for the carbon fiber material, respectively. $a = \pi r^2$, $I = \pi r^4/4$, and $r = 0.25$mm are the beam cross-section area, second moment of area, and radius, respectively.

Eq. 3 is a 4th-order differential equation that presents the balance between the distributed loads, e.g. beam mass, along the beam. The balance of local shear loads, e.g. point masses and contacting springs, along the beam can be presented with a set of 3rd-order differential equations. The effect of the attached springs to the beam that exert point loads at their contacting locations are captured as boundary conditions in these 3rd-order differential equations. The boundary conditions related to the base linear ($k_1 = 0.2$N/mm) and torsion ($k_\theta = 200$Nm/rad) springs, and the stiffness variable linear spring (k_f) are given by load balance equations at the spring attachment points as [22], [23]:

$$EI\partial^3 w(L)/\partial x^3 + k_1 w(L) = 0, \tag{4}$$
$$EI\partial^2 w(L)/\partial x^2 - k_\theta \partial w(L)/\partial x = 0,$$
$$EI\partial^3 w(D)/\partial x^3 + k_f w(D) = 0,$$

The balance of moment is presented with a 2nd-order differential equation. The local shear force and moment are zero at the beam boundary conditions. Hence, the free ends boundary conditions can be derived as:

$$\partial^3 w(0|P)/\partial x^3 = \partial^2 w(0|P)/\partial x^2 = 0, \tag{5}$$

where $L = 8$mm, $D = 13$mm, and $P = 213$mm are the position of the silicone joint, the piezoelectric sensor and the overall length of the beam, respectively. The time derivatives are not present here due to lack of any point load along the beam (The sensors are considered to have zero masses). These boundary conditions are valid at any time.

To find the beam natural frequencies (ω_n) and mode shapes (W_{ω_n}), we neglect $F(x,t)$ and follow the method of separation of variables by setting $w(x,t) = W(x)T(t)$, where $W(x)$ is a function that depends only on the spatial variable x and $G(t)$ is a function that depends only on the temporal variable t. By substituting the resulting system constant with $-\omega_n^2$, a Boundary Value Problem (BVP) can be expressed for $W(x)$ as follows [22]:

$$EI\,\text{d}^4 W/\text{d}x^4 - \rho a \omega^2 W = 0. \tag{6}$$

To be solved this BVP, the Matlab "bvp5c" function [23] have been used. The simulation parameters are chosen to closely match our experiment conditions.

The simulation results in Fig. 3 illustrate the mode shapes and correlation between the induced piezoelectric sensor stress (σ_{PS}) and the Hall effect sensor flux (B_{H}) against the follicle stiffness (found from experiments) for three different natural
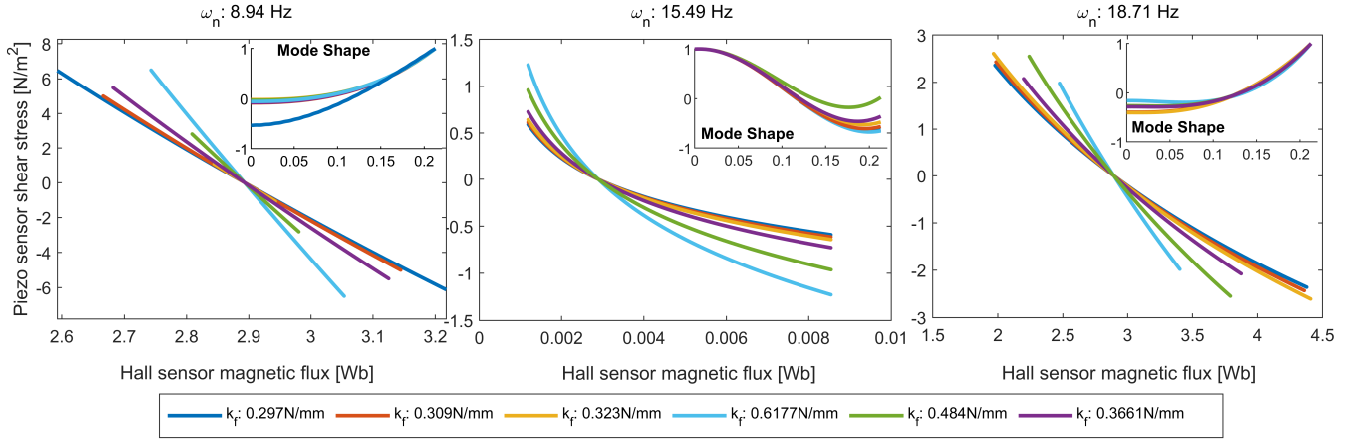
Fig. 3: Simulated correlation between the induced piezoelectric sensor stress (σ_{PS}) and the Hall effect sensor flux (B_{H}) against the follicle stiffness for three different natural frequencies (ω_n) and $w_{\max} = 5$mm. Notice the different axes scales.
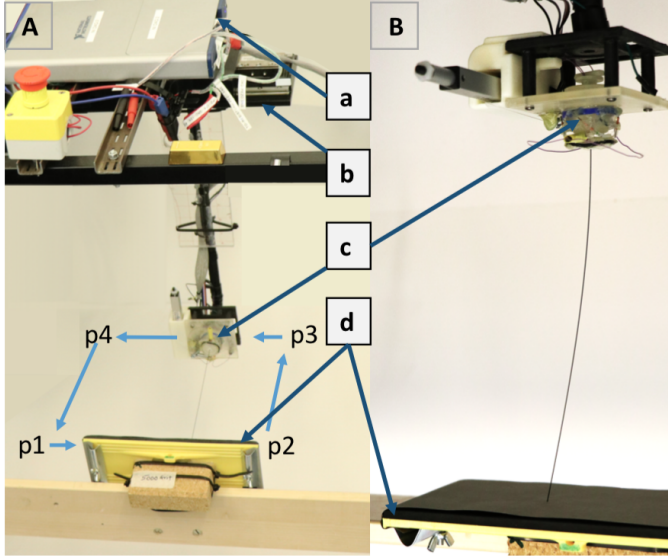

Fig. 4: Experimental Setup (A) Hardware Setup and Programmed Path: (a) Data acquisition system (DAQ); (b) XY linear stage; (c) variable stiffness multimodal whisker follicle (VS-MWF); (d) Sandpaper holder; Programmed Path is $p1$, $p2$, $p3$ and $p4$ (Data is recorded only when the Whisker shaft moves from $p1$ to $p2$). (B) VS-MWF probing against a sandpaper.

frequencies ($\omega_n \approx [8.9, 15.5, 18.7]$ Hz) and $w_{\max} = 1$mm. These results show that the correlation between the sensors reading may significantly change depending on the natural frequency of the system dominant mode of vibration. Also, the change of the follicle stiffness significantly affects the correlation between both sensors and the beam mode shape for the same natural frequency. This means that the follicle sensitivity can be changed by controlling the stiffness of the whisker follicle.

D. Experiment Setup

The experimental setup is shown in Fig. 4. The whisker sensor is horizontally attached to a 3D printed ABS plastic

holder. This holder is connected to a 36cm L-shape rigid copper pipe arm whose longest side is strengthened using an acrylic sheet. The end corresponding to the longest side of this arm is attached to the XY stage (Aerotech- ANT130-160-XY) through a $70{\times}70{\times}5$mm rigid 3D printed ABS plastic plate. This stage allows controlling the movement of the whisker sensor along the **x** and **y** coordinates.
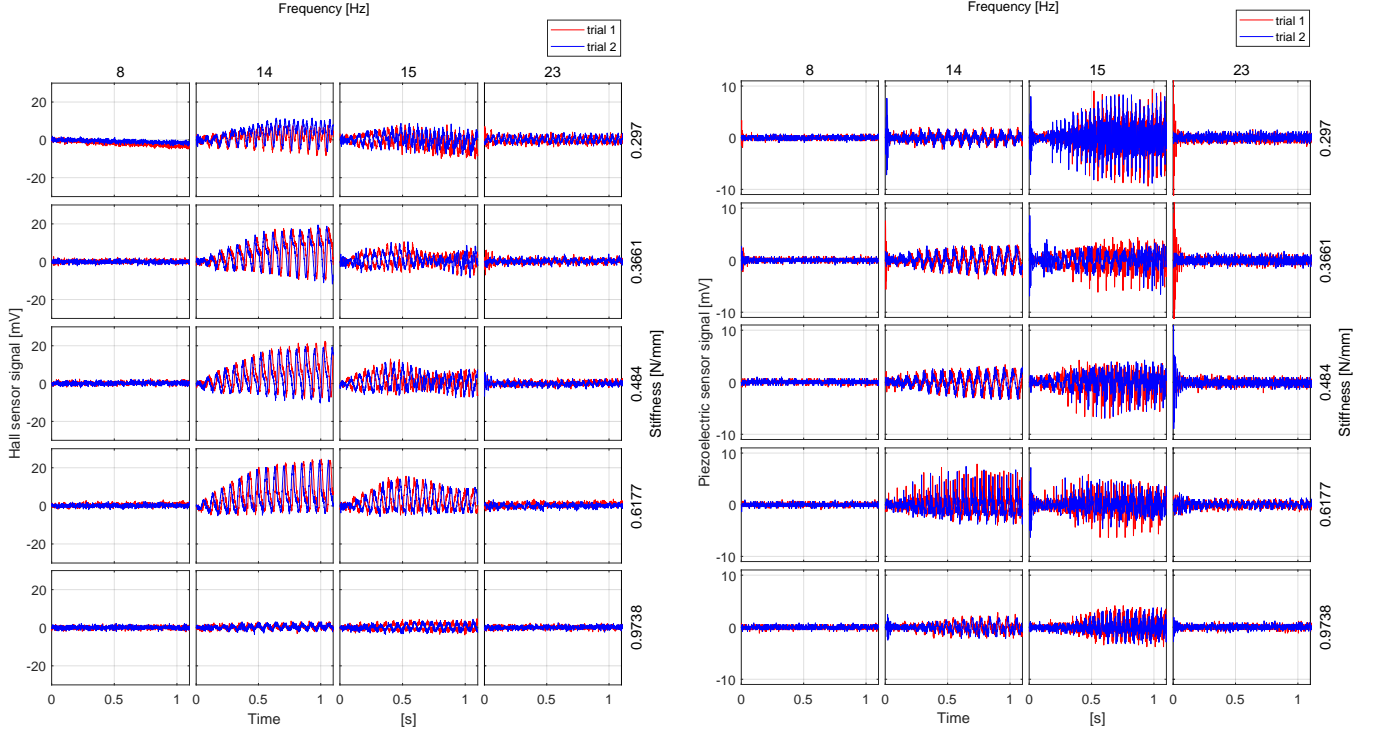
A National Instrument NI DAQ USB-6341 Multifunction I/O Device together with a LabView2016 interface was used to acquire signals from the whisker sensor at a 10kHz sampling rate and to control the RRM, and XY linear stage. MatLab R2016a, Mathworks Inc, was employed for the post-processing and analysis of the data.

1) Experiment-1: Characterization of the natural frequency of the VS-MWF: In this initial experiment, the whisker follicle was vibrated for 30 cycles from 8Hz to 23Hz in 1Hz steps (16 frequency steps in total) to understand the frequency response of the free whisker and follicle (whisker not touching a surface). The magnitude of oscillation along the y-axis of the stage has been chosen arbitrarily at 0.5mm.

In this experiment, we use stiffnesses 0.2970, 0.3090, 0.3230, 0.3661 ,0.4840, 0.6177, 0.8328, 0.9622 and 0.9738N/mm for each frequency. Initially, the stiffness is set to 0.2970N/mm (carbon shafts inserted at the lowest level into the silicone tubes attached to the WSB joint), which provides a default stiffness of the silicone joint. The corresponding initial frequency of the whisker sensor is set to 8Hz. In a set of trials, the whisker vibrates 30 cycles, then stops and stabilizes at its initial position. For each combination of stiffness levels and frequency levels, we acquired data for 2 trials of 30 cycles each.

We took the first 100 samples (10ms) in each trial to compute the base level readings of both the Hall and piezoelectric sensors and subtracted this from the raw data to obtain signals that are caused due to the oscillations.

2) Experiment-2: The behavior of the VS-MWF in texture discrimination : In the second experiment, the whisker was programmed to probe along the rough side of 12 sandpaper samples (80, 240, 320, 400, 600, 800, 1000, 1200, 2000, 3000, 5000, 7000 grit roughness) for a 7.5cm span as shown in Fig.

(a) Raw data of Hall effect sensor for different frequencies and stiffness.

(b) Raw data of piezoelectric sensor for different frequencies and stiffness.

Fig. 5: Raw data acquired for the two sensors for different frequencies and stiffnesses

4. The whisker was moved to the edge of a sandpaper holder with an indention of 3mm before starting to sweep across the sandpaper at different speeds. We chose a 3mm indentation based on our previous results [19].

In the experiment, one sandpaper sample is fixed to the external holder and clamped perpendicular to the whisker shaft (Fig. 4). Initialization of the experiment for each sandpaper sample is identical for all the iterations. By following the path shown in Fig. 4.A, the whisker sensor comes into contact with the surface of the sandpaper. These movements are controlled through the usage of the XY stage. The stiffness of the whisker follicle use the following values 0.2970, 0.3090, 0.3230, 0.3661, 0.4840, 0.6177, 0.8328, 0.9622 and 0.9738 N/mm similar to the II-D1. In this experiment, we use 3mm contact indentation across all iterations and 10mm/s, 14mm/s, 18mm/s, whisking speeds. Initially, the stiffness is set to 0.2970N/mm, as the default stiffness of the silicone joint between the two sensors of the whisker follicle and the corresponding whisking speed of the whisker sensor is set to 10mm/s. For each combination of stiffness levels and contact speed, we acquired data for 2 trials. Therefore, for a given stiffness, the three contact speeds gave 6 data sets for a single sandpaper.

E. calculation of distance between distribution of textures

We took base subtracted data as described in the last paragraph of section II-D1. The Hall and piezoelectric sensor data were divided into 200 bins to construct a distribution of root mean square (RMS) values to compare two textures. A distance metric between these distributions for two textures was computed to understand how the follicle stiffness and whisking speed influences the distance metric.

We quantify distance between RMS distributions of textures A and B, using the standardized Euclidean Distance (SED) given by

$$SED_{AB} = \sqrt{\frac{\Sigma(\mathbf{RMS_A} - \mathbf{RMS_B})^2}{\sigma_A \sigma_B}} \qquad (7)$$

where, $\mathbf{RMS_A}$ is a vector of RMS values of sensor readings in 200 time bins when the whisker is brushed on one material (12 sandpapers from 80 - 7000 grit) and $\mathbf{RMS_B}$ is that for the reference sample (80 grit sandpaper). The corresponding standard deviations are σ_A and σ_B. In our case, SED_{AB} is the standardized Euclidean Distance between the RMS values of sensor data across 200 bins in a given brushing trial corresponding to two sandpapers. We used normalized SED, hereafter referred as $NSED$ for clarity of comparison.

III. RESULTS

A. Numerical simulation results

Fig. 3 shows numerical simulation results based on the model derived in section II-C. The analytical model predicts that stiffness can be used to rotate the covariance between the Hall effect sensor and the piezoelectric sensor for a given
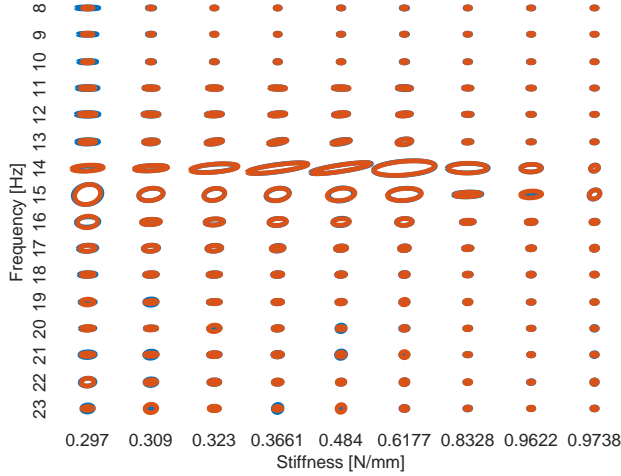
Fig. 6: Covariance of Piezoelectric and Hall effect sensor signals for different combinations of stiffness and frequency for free whisker (whisker not touching a surface) and follicle vibrations . Red and blue ellipses refer to trials 1 and 2, respectively. Axes ranges are not shown for clarity. x and y axes are normalized to respect the aspect ratio. The range of the axes are from -0.0210 to 0.0210 and from -0.0069 to 0.0069 respectively for x and y. The shape of the ellipsoids represents the Eigenvalues of the principal components of each covariance matrix.

whisker vibration. In other words, the stiffness of the follicle is a useful internal parameter to bias perception in the frequency domain.

B. Signal amplitude variation with follicle stiffness and free oscillation frequency

Fig. 5a and Fig. 5b show the base subtracted raw experimental readings (see section II-D1 in the methods section for details) from the Hall effect sensor and the piezoelectric sensor mounted in the VS-MWF for selected levels of oscillation frequencies (8, 14, 15 and 23 Hz) and stiffnesses 0.2970, 0.3661, 0.4840, 0.6177 and 0.9738 N/mm. We can observe a higher magnitude in the signals for 14-15Hz oscillation frequency. We can also see that the magnitude variation is depending on the stiffness of the VS-MWF. Fig. 6 shows the covariance ellipses between the two sensor modalities for different combinations of follicle stiffness and oscillation frequencies. The variation of the size of the ellipses shows that follicle stiffness helps to rotate the Eigenvectors of the covariance matrix and that the maximum Eigenvalues correspond to oscillation frequencies between 12 - 16Hz.

These results provide important clues to acquire information in the frequency domain for texture classification by maximizing the signal to noise ratio of measurements. To demonstrate this effect, we did a second experiment that involves distinguishing 12 pairs of sandpapers (80 - 7000 grit) described in more detail in section II-D2.
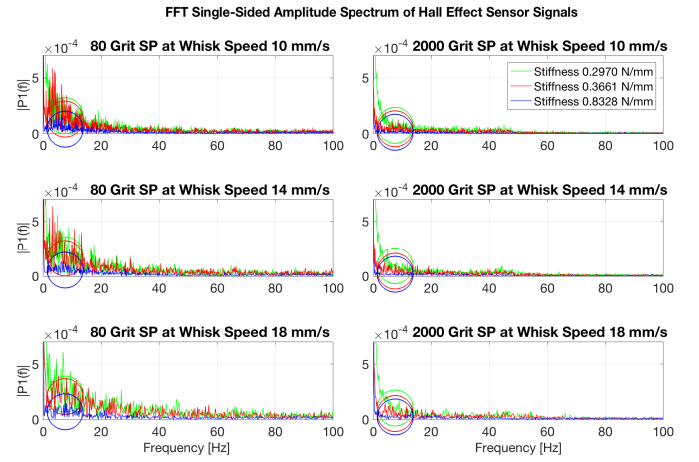

Fig. 7: FFT of Hall effect sensor data at follicle stiffness 0.2970N/mm, 0.3661N/mm,0.8328N/mm and whisking speed 10mm/sec,14mm/sec ,18mm/sec on 80, 2000 grit sandpapers.
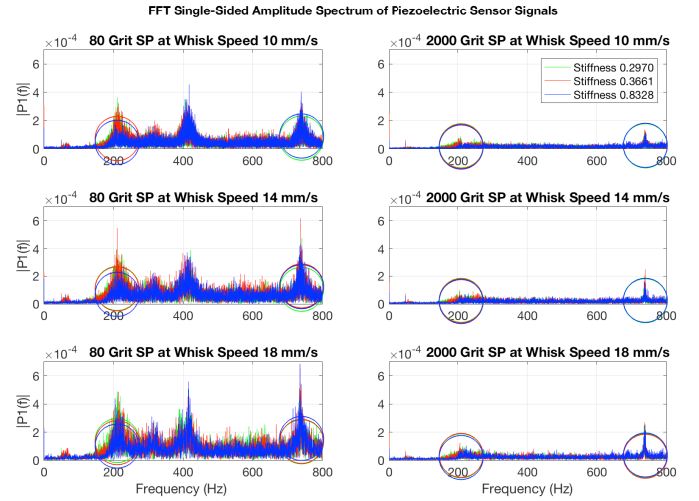

Fig. 8: FFT of Piezoelectric sensor data at follicle stiffness 0.2970N/mm, 0.3661N/mm,0.8328N/mm and whisking speed 10mm/sec,14mm/sec ,18mm/sec on 80, 2000 grit sandpapers.

C. Maximizing a difference metric for texture classification

Fig. 7 and Fig. 8 show the fast Fourier transform (FFT) single-sided amplitude spectrum of the Hall effect sensor and Piezoelectric sensor signals at 0.2970N/mm, 0.3661N/mm, 0.8328N/mm follicle stiffness and whisking speeds 10mm/sec, 14mm/sec ,18mm/sec on 80, 2000 grit sandpapers. Here we can notice that the hall effect sensor produces high power amplitude in the low-frequency region ($0 - 40$ Hz) and Piezoelectric sensor produces high power amplitude in the high-frequency region (100 Hz and above). The circles show the median value of the particular distribution at above described follicle stiffness values. The circles show the hall effect sensor produces high power low frequency components at low stiffness values. Moreover, the hall effect sensor FFT shows a frequency shift with the change of stiffness. The circles on Fig. 8 shows that the piezoelectric sensor produces low power low frequency components and high power high
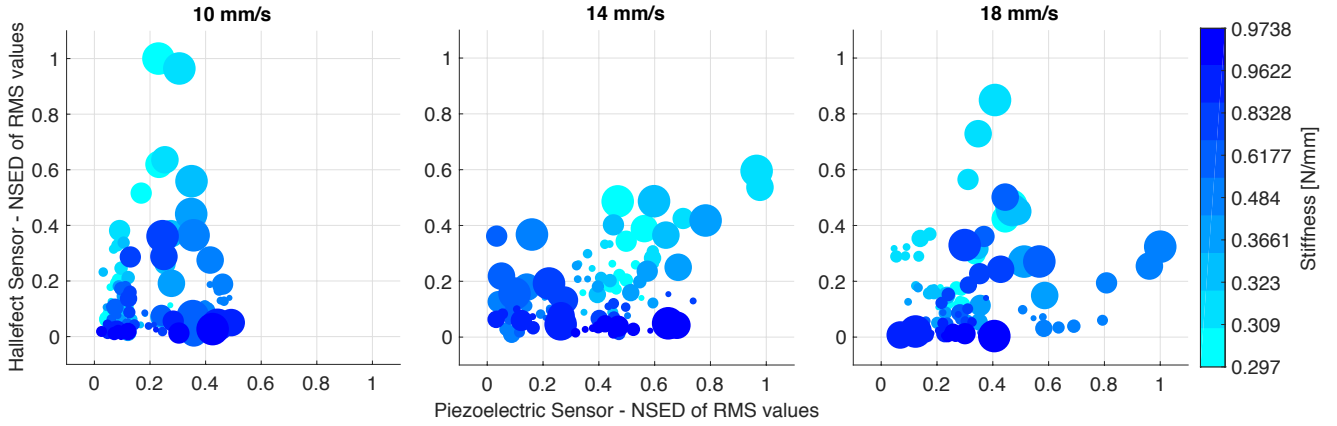
Fig. 9: NSED - Normalize Standardized Euclidean Distance of RMS values computed using equation (7). The smallest circle represent the rough sandpaper, and the largest circle represent the smoothest sandpaper. At a given speed, the Standardized Euclidean Distance of the RMS values used to compare between roughest sandpaper (80 grit) against all other sandpapers. The sandpaper grit values are 80, 240, 320, 400, 600, 800, 1000, 1200, 2000, 3000, 5000, 7000.

frequency components. This effect increases with increasing follicle stiffness. Interestingly, with low stiffness, it produces high power amplitude on low frequencies and low power amplitude on high frequencies. Therefore, the piezoelectric sensor with variable stiffness contributes to filter signals. This phenomenon implies that the interaction effect of the speed of whisking with follicle stiffness help to capture information in different frequency components in the frequency domain and for the texture classification task.

Fig. 9 Shows the NSED of RMS values of the Hall-effect sensor and the Piezoelectric sensor data of 12 different grit level of sandpapers at nine stiffnesses 0.2970, 0.3090, 0.3230, 0.3661, 0.4840, 0.6177,0.8328, 0.9622, 0.9738 N/mm and three whisking speeds of 10, 14, 18 mm/s. The largest circles represent the smoothest (7000 grit) sandpaper, and the smallest represent the rough (240 grit) sandpaper. The RMS values of the two sensor modalities corresponding to the 80 grit sandpaper were used as the reference to compute the NSED for all other sandpapers.

The study shows that the sensor at the low whisking speed at low stiffness favor the hall effect sensor by producing a higher NSED. Moreover, when the whisking speed and stiffness increases, NSED of piezoelectric sensor increases disproportionately compared to the Hall effect sensor. Essentially the follicle stiffness allows the sensor to bias itself in the frequency domain for the given speed of whisking.

This observation also shows that the Hall effect sensor capture the low-frequency region (i.e. the geometric features of an object) and the piezoelectric sensor capture the high-frequency region (i.e. the texture of objects) . The substantial benefit of using the multimodal follicle is therefore being able to capture different vibration frequencies by controlling the stiffness of the follicle together with the whisking speed. This is very useful for a robot to acquire texture and geometry information of an object realtime.

These insights show that a robot using a rat whisker inspired VS-MWF can improve the efficiency of identifying objects by

exploiting the interaction effect of whisking speed and the stiffness of the follicle that houses multiple modes of sensors with a multi-modal whisker follicle.

IV. DISCUSSION AND CONCLUSION

In this paper, we tested a novel variable stiffness multimodal whisker sensor (VS-MWS) for its ability to distinguish pairs of sandpapers for different follicle stiffnesses and whisking speeds. We used sandpapers because their smoothness can be quantified using the grit number. Our experimental results show for the first time that a multimodal sensor can help to move the bandwidth of signal gain from low to high frequency information of textures by changing the stiffness and whisking speed. In particular, our findings show that the efficacy of robotic whiskers can be improved by using multi-modal transduction embedded in a controllable stiffness follicle, whereby the vibration dynamics of the follicle can be used to induce mutual information that the sensors cannot acquire in isolation. These findings provide important design guidelines for whisker sensors in future robots to identify texture and geometry information of objects.

There are several previous studies that consider the role of whisker shaft stiffness and the probing pattern in tactile sensing. For instance, authors in [24] observed that a stiffer whisker would increase the sensitivity of a piezoelectric transducer attached to the whisker. Pearson et. al., described a biomimetic whisking pattern [12], and Sornkarn [25] found that the internal stiffness of a probe can help to gain information during soft tissue palpation. Our findings consolidate those in [25] in a multimodal sensing context.

In addition to implications in robotics, these findings also make predictions about the rat whisker follicles. Authors in [26] have found that the morphology and mechanics provide the basis for a pre-neural computation of rat vibrissal information (afferent signals). However, the contribution of the ring muscle structure between the superficial and deep vibrissal nerves of the rat whisker follicle in terms of capture

information has not been fully understood so far [26] [6] [27]. The findings in this paper predict that this mechanism to control the stiffness of the follicle may lead to capture information across a broad frequency spectrum using a controllable stiffness whisker follicle.

In conclusion, this paper for the first time delivers substantial insights into how the stiffness control in a whisker follicle is associated with multiple sensory information capture in texture classification.

REFERENCES

[1] G. E. Carvell and D. J. Simons, "Biometric analyses of vibrissal tactile discrimination in the rat," *Journal of Neuroscience*, vol. 10, no. 8, pp. 2638–2648, 1990.

[2] A. S. Ahl, "The role of vibrissae in behavior - a status review." *Veterinary Research Communications*, vol. 10, no. 4, pp. 245–268, 1986.

[3] H. Takahashi-Iwanaga, "Three-dimensional microanatomy of longitudinal lanceolate endings in rat vibrissae," *Journal of Comparative Neurology*, vol. 426, no. 2, pp. 259–269, 2000.

[4] F. L. Rice, A. Mance, and B. L. Munger, "A comparative light microscopic analysis of the sensory innervation of the mystacial pad. i. innervation of vibrissal follicle-sinus complexes," *Journal of Comparative Neurology*, vol. 252, no. 2, pp. 154–174, 1986.

[5] M. Szwed, K. Bagdasarian, and E. Ahissar, "Encoding of vibrissal active touch," *Neuron*, vol. 40, no. 3, pp. 621–630, 2003.

[6] J.-N. Kim, K.-S. Koh, E. Lee, S.-C. Park, and W.-C. Song, "The morphology of the rat vibrissal follicle-sinus complex revealed by three-dimensional computer-aided reconstruction," *Cells Tissues Organs*, vol. 193, no. 3, pp. 207–214, 2011.

[7] L. Pammer, D. H. O'Connor, S. A. Hires, N. G. Clack, D. Huber, E. W. Myers, and K. Svoboda, "The mechanical variables underlying object localization along the axis of the whisker," *Journal of Neuroscience*, vol. 33, no. 16, pp. 6726–6741, 2013.

[8] R. A. Russell, "Closing the sensor-computer-robot control loop," *Robotics Age*, vol. 6, no. 4, pp. 15–20, 1984.

[9] R. A. Russell and J. A. Wijaya, "Object exploration using whisker sensors," *Australasian Conference on Robotics and Automation*, pp. 180–185, 2002.

[10] M. Fend, "Whisker-based texture discrimination on a mobile robot," *Advances in Artificial Life*, vol. 3630 of the series Lecture Notes in Computer Science, pp. 302–311, 2005.

[11] J. H. Solomon and M. J. Hartmann, "Robotic whiskers used to sense features," *Nature*, vol. 443, no. 7111, p. 525, 2006.

[12] M. Pearson, B. Mitchinson, *et al.*, "Biomimetic vibrissal sensing for robots." *Phil. Trans. R. Soc. B*, vol. 366, no. 1581, 2011.

[13] J. H. Solomon and M. J. Hartmann, "Artificial whiskers suitable for array implementation: accounting for lateral slip and surface friction," *IEEE Transactions on Robotics*, vol. 24, no. 5, pp. 1157–1167, 2008.

[14] D. Kim and R. Moller, "Biomimetic whiskers for shape recognition," *Robotics and Autonomous Systems*, vol. 55, no. 3, pp. 229–243, 2007.

[15] A. Kottapalli, M. Asadnia, J. Miao, and M. Triantafyllou, "Harbor seal whisker inspired flow sensors to reduce vortex-induced vibrations," in *2015 28th IEEE International Conference on Micro Electro Mechanical Systems (MEMS)*. IEEE, 2015, pp. 889–892.

[16] N. Sornkarn, M. Howard, and T. Nanayakkara, "Internal impedance control helps information gain in embodied perception," in *Robotics and Automation (ICRA), 2014 IEEE International Conference on*. IEEE, 2014, pp. 6685–6690.

[17] J. Sullivan, M. Pearson, *et al.*, "Tactile discrimination using active whisker sensors," *IEEE Sensors*, vol. 12, no. 2, pp. 350–362, 2012.

[18] L. A. Huet, J. W. Rudnicki, and M. J. Hartmann, "Tactile sensing with whiskers of various shapes: Determining the three-dimensional location of object contact based on mechanical signals at the whisker base," *Soft Robotics*, vol. 4, no. 2, pp. 88–102, 2017.

[19] H. Wegiriya, N. Sornkarn, H. Bedford, and T. Nanayakkara, "A biologically inspired multimodal whisker follicle," in *Systems, Man, and Cybernetics (SMC), 2016 IEEE International Conference on*. IEEE, 2016, pp. 003 847–003 852.

[20] T. J. Park, C. Comer, A. Carol, Y. Lu, H.-S. Hong, and F. L. Rice, "Somatosensory organization and behavior in naked mole-rats: Ii. peripheral structures, innervation, and selective lack of neuropeptides associated with thermoregulation and pain," *Journal of comparative neurology*, vol. 465, no. 1, pp. 104–120, 2003.

[21] M. Baatz and M. Hyrenbach, "Method of calculating the magnetic flux density and forces in contactfree magnetic bearings," July 1991. [Online]. Available: https://onlinelibrary.wiley.com/doi/abs/10.1002/etep.4450010404

[22] B. Balachandran and E. B. Magrab, *Vibrations*, 2nd ed. Australia: Cengage Learning, 2009, oCLC: ocn181603380.

[23] E. B. Magrab, *An engineer's guide to MATLAB: with applications from mechanical, aerospace, electrical, civil, and biological systems engineering*, 3rd ed. Upper Saddle River, N.J: Prentice Hall, 2011, oCLC: ocn465867437.

[24] F. Ju and S.-F. Ling, "Bioinspired active whisker sensor for robotic vibrissal tactile sensing," *Smart Materials and Structures*, vol. 23, no. 12, p. 125003, 2014.

[25] N. Sornkarn and T. Nanayakkara, "The efficacy of interaction behavior and internal stiffness control for embodied information gain in haptic perception," in *Robotics and Automation (ICRA), 2016 IEEE International Conference on*. IEEE, 2016, pp. 2657–2662.

[26] A. Wallach, K. Bagdasarian, and E. Ahissar, "On-going computation of whisking phase by mechanoreceptors," *Nature neuroscience*, vol. 19, no. 3, p. 487, 2016.

[27] E. Arabzadeh, R. S. Petersen, and M. E. Diamond, "Encoding of whisker vibration by rat barrel cortex neurons: implications for texture discrimination," *Journal of Neuroscience*, vol. 23, no. 27, pp. 9146–9154, 2003.